ACS APPLIED MATERIALS & INTERFACES

Research Article

www.acsami.org

Solution-Processed Organic Solar Cells from Dye Molecules: An Investigation of Diketopyrrolopyrrole:Vinazene Heterojunctions

Bright Walker,[†] Xu Han,[‡] Chunki Kim,[†] Alan Sellinger,[‡] and Thuc-Quyen Nguyen*[,†]

[†]Departments of Chemistry and Biochemistry, Center for Polymers and Organic Solids, University of California, Santa Barbara, California 93106, United States

[‡]Department of Materials Science and Engineering, Center for Advanced Molecular Photovoltaics (CAMP), Stanford University, Stanford, California 94305, United States

Supporting Information

ABSTRACT: Although one of the most attractive aspects of organic solar cells is their low cost and ease of fabrication, the active materials incorporated into the vast majority of reported bulk heterojunction (BHJ) solar cells include a semiconducting polymer and a fullerene derivative, classes of materials which are both typically difficult and expensive to prepare. In this study, we demonstrate that effective BHJs can be fabricated from two easily synthesized dye molecules. Solar cells incorporating a diketopyrrolopyrrole (DPP)-based molecule as a donor and a dicyanoimidazole (Vinazene) acceptor function as an active layer in BHJ solar cells, producing relatively high open circuit voltages and power conversion efficiencies (PCEs) up to 1.1%. Atomic force microscope images of the films show that active layers are rough and apparently have large donor and acceptor domains on the surface, whereas photoluminescence of the blends is incompletely quenched, suggesting that higher PCEs might be obtained if the morphology could be improved to yield smaller domain sizes and a larger interfacial area between donor and acceptor phases.

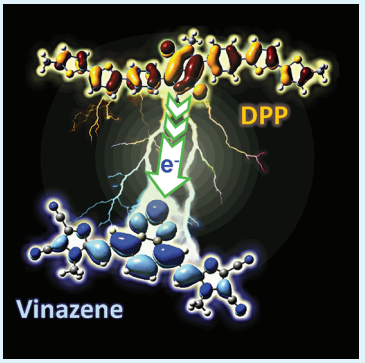

KEYWORDS: *dicyanoimidazole, Vinazene, diketopyrrolopyrrole, DPP, organic solar cell, bulk heterojunction*

INTRODUCTION

In recent years, there has been growing evidence that organic solar cells have lifetimes and power conversion efficiencies (PCEs) large enough to make them useful power sources.[1−4] Given their potential to be manufactured at a relatively low cost, along with their lightweight, aesthetic properties and flexibility, they have significant advantages compared to other solar technologies and are gaining appeal as a commercially viable technology. Interest in the field has seen tremendous growth in the past decade as reported lifetimes and PCEs have increased rapidly.[5]

Although progress has been rapid, there are many shortcomings that need further improvement before organic solar cells can be widely commercialized. In the case of solution-processed bulk heterojunction (BHJ) solar cells, the active materials reported in efficient designs almost exclusively include a conjugated polymer donor and a fullerene acceptor,[6−8] both of which are typically synthesized by low yielding reactions, involve difficult purification procedures and large volumes of organic solvents. Furthermore, as polymers generally are less pure and have many more variables than small molecules, i.e., varying molecular weights (MW), polydispersities (PDI), defects within the polymer backbone, removal of residual metal catalysts/ligands, strong dependence on solvent, etc., it is common that the same polymer can have different properties between synthesized batches.

Although conjugated polymers have so far given the best results as donor materials in BHJs, it is also possible to fabricate BHJs using small molecule donors, which are generally easier to synthesize and purify than their polymeric counterparts.[9−18] In this line of work, our group has investigated the use of diketopyrrolopyrrole (DPP) based molecular semiconductors as donor materials in BHJ solar cells. Fullerene derivatives have so far given the best performance as acceptors in BHJ solar cells, but their syntheses involve low yielding combustion reactions, laser ablation techniques and/or complex synthetic schemes and extensive purifications.[19] Alternatives to fullerenes have also been demonstrated, although typically with lower PCEs.[20−26]

In this contribution, we demonstrate that the active layer in BHJ solar cells can be prepared from two easily synthesized molecules, including a DPP donor and dicyanoimidazolyl (Vinazene) acceptor. Optimized devices using these materials in BHJ or bilayer heterojunction configurations produce open circuit voltages (V_{OC}) in the range of about 1.08 to 1.25 V. Although the PCEs are modest, it is possible that improvements to material design and device processing may enable higher efficiencies.

RESULTS AND DISCUSSION

Two donors (**D1** and **D2**) and two acceptors (**A1** and **A2**) were explored in this study; the structures are shown in

Received: September 23, 2011
Accepted: December 2, 2011
Published: December 2, 2011

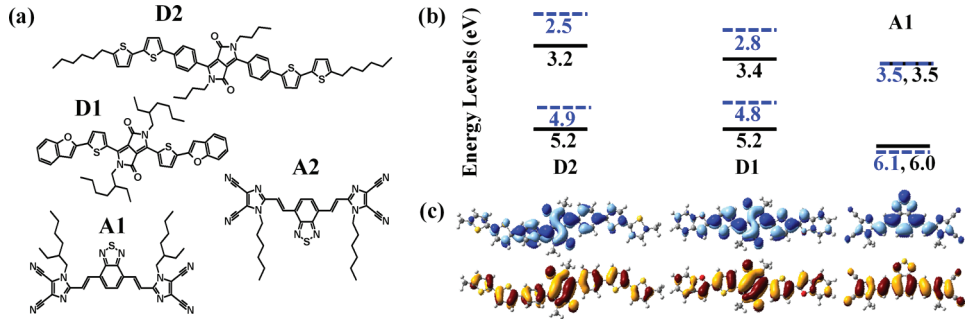

Figure 1. (a) Structures and (b) energy levels of the materials as calculated by DFT (blue dotted lines) or as measured by photoemission spectroscopy (solid black lines). DFT was used to calculate (c) the geometries of the frontier orbitals where the HOMO orbitals (bottom) are represented by a red/yellow color scheme and the LUMO orbitals (top) are represented by a blue/aqua color scheme.

Figure 1a. **D1** was chosen as it has yielded the best results out of the DPP-cored small molecule donors that our group has explored.[27] **D2** was selected as it has a somewhat higher lying lowest unoccupied molecular orbital (LUMO) level to facilitate electron transfer to the Vinazene acceptor. The donors were synthesized in four steps, beginning with formation of the DPP core via the base-catalyzed condensation of dibutyl succinate and an aryl nitrile, followed by alkylation of the lactam nitrogen, bromination with NBS and Suzuki coupling of the resulting compound with the appropriate aryl boronic acid.[28] The acceptors were also readily synthesized by first alkylating 2-vinyl-4,5-dicyanoimidazole using the appropriate alkyl bromide followed by Heck coupling with 4,7-dibromo-2,1,3-benzothiadiazole.[22]

The conjugated cores of the compounds were simulated via density functional theory (DFT), using Beck's 3-parameter [Lee, Yang, Parr] basis set (B3LYP) at the 6-31G(d,p) level of theory.[29] The n-hexyl and 2-ethylhexyl chains were truncated to methyl groups in order to reduce computation time. The energy levels are reported as blue dotted lines in Figure 1b, whereas the highest occupied molecular orbital (HOMO) and LUMO are shown in Figure 1c as yellow/orange and blue/aqua shapes, respectively. The materials were characterized by photoemission spectroscopy to determine their ionization potentials or HOMOs. Both DPP materials show delocalization of the HOMO orbitals over the entire molecule, whereas the LUMO is somewhat more confined to the DPP core and first adjacent rings. The optimized geometry of the **D1** material shows that it is almost completely planar, while the phenyl groups in **D2** are twisted somewhat out of plane relative to the DPP core, which appears to destabilize the LUMO slightly without greatly affecting the energy of the HOMO. Films of **D1** and **D2** were analyzed by Ultraviolet Photoemission Spectroscopy (UPS) while the ionization potential of **A1** was measured by photoemission spectroscopy in air (PESA). These values were taken as HOMO energies, while LUMO energies were estimated by subtracting the optical band gap taken from absorption spectra. The observed energy levels are reported as black, solid lines in Figure 1b.

DFT calculations predict that both DPP materials should have similar HOMO levels, whereas **D1** is expected to have a deeper LUMO and smaller band gap. These trends are confirmed by UPS and thin film absorption; we see that **D1** has a smaller optical band gap than **D2** (1.7 eV vs 1.9 eV, respectively), with broader absorption (absorption onsets of 650 nm (Figure 2a) and 710 nm[27] for **D2** and **D1**, respectively) and a more stable LUMO than **D2** (3.2 and 3.4 eV for **D2** and **D1**, respectively). However, the absolute values are shifted somewhat in the solid state compared to the gas-phase calculations. For films of both materials, the energy levels are deeper, whereas the band gaps are smaller than those predicted by DFT, a shift that can be attributed to aggregation and delocalization of orbitals in the solid state.[30−32]

DFT predicts that the Vinazene materials should have somewhat deeper energy levels, with a HOMO and LUMO of 6.1 and 3.5 eV, respectively. PESA and the optical band gap of films of the material indicate that the energy levels in the solid state are quite similar to the values predicted by DFT. Indeed, comparing the absorption of **A1** in solution[22] to the solid-state absorption (Figure 2a) shows that there is little difference in spectral shape or absorption onset, suggesting that the frontier orbitals of **A1** are not greatly affected by aggregation or delocalization effects in the solid state. The geometries of the Vinazene orbitals show that both the HOMO and the LUMO are delocalized over most of the molecule.

From the measured energy levels in the solid state, we find that LUMO−LUMO offset of **D1** and **A1** is only about 0.1 eV, which may be too small to allow efficient photoinduced electron transfer. However, the LUMO−LUMO offset **D2** and **A1** is 0.3 eV, which should provide enough driving force for charge separation. The difference between the LUMO of **A1** and the HOMO of **D2**, minus a correction factor of 0.3 V, gives a predicted approximate V_{OC} of 1.4 V.[33] While photoelectron spectroscopy constitutes a common technique used to measure energy levels, cyclic voltammetry (CV) represents another popular method and was used to confirm our photoelectron results. Voltammograms were collected for both **D2** and **D1**, and compared to previously reported CV values for **A1**; these data are reported in the Supporting Information (Figure S1). Although the band gaps of the donors as observed by CV are slightly larger than those obtained from the visible absorption onsets, the CV data also indicate similar trends as those predicted by UPS; a large V_{OC} is predicted based on the HOMO of **D2** and LUMO of **A1**, while there is essentially no LUMO−LUMO offset to drive electron transfer from **D1 to A1**. Indeed, the **D1:A1** devices show very poor performance (see the Supporting Information, Figure S2), while the **D2** devices show V_{OC} vaules of up to 1.25 V, which will be discussed in greater detail later.

Examining the absorption spectra in Figure 2a show that **D2** has strong absorption bands at 400 nm and from 550 to 650 nm, with little change upon annealing at 100 °C, whereas **A1** shows strong absorption at 350 and 450 nm. The spectrum of **A1** begins to show some tapering into the IR region after

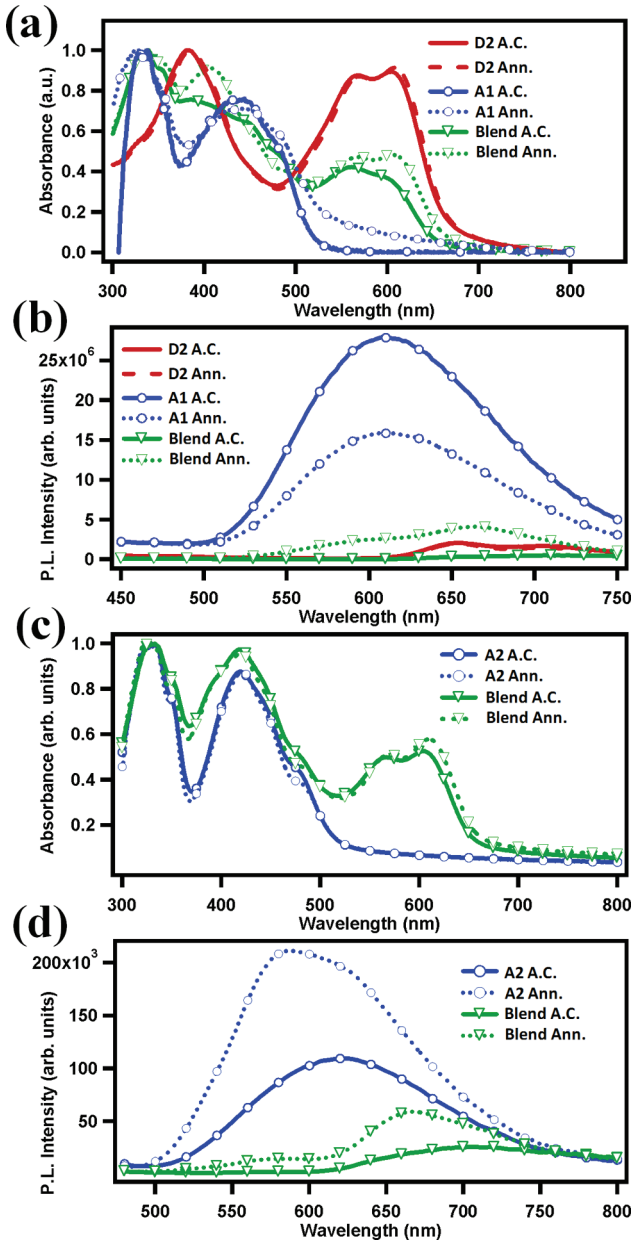

Figure 2. (a, c) Absorption and (b, d) fluorescence spectra of as-cast (solid lines) and annealed (dashed lines) of **D2** (red), and **D2**:Vinazene mixtures (green). Absorption and fluorescence spectra of **A1** (blue) and 1:1 mixture of **D2** and **A1** (green) are plotted in a and b, whereas absorption and fluorescence spectra of **A2** (blue) and 1:1 mixture of **D2** and **A2** are plotted in c and d, respectively.

annealing, indicative of light scattering and/or the formation of larger aggregates which are apparent in atomic force microscope (AFM) images (discussed later). Blends of the materials absorb strongly in the range of 300 to 650 nm, showing an increase in absorption intensity at 400 and 600 nm regions upon annealing. These peaks correspond to **D2** and suggest an increase in the optical density of the material after thermal annealing, an effect which has been previously observed with **D1** and its blends with $PC_{71}BM$.[27]

The photoluminescence (PL) of the materials was also examined and plots of PL intensity versus wavelength are reported in Figure 2b. Pure films of **D2** show weak fluorescence in the solid state which is not affected by annealing at 110 °C.

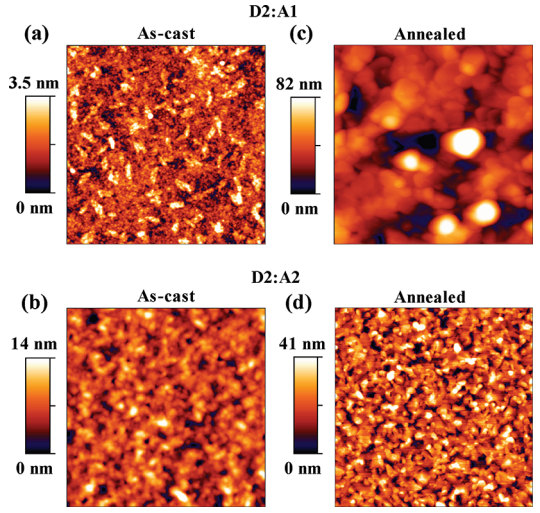

Figure 3. AFM images of 1:1 mixtures of (a, c) **D2**:**A1** and (b, d) **D2**:**A2** (a, b) before and (c, d) after annealing at 110 °C for 10 min in a nitrogen environment.

A1 shows considerably stronger fluorescence, which decreases significantly after thermal annealing at 110 °C. This decrease in fluorescence intensity can be attributed to aggregation induced quenching;[34] although annealing does not alter the absorption spectrum considerably, the higher degree of aggregation appears to reduce the efficiency of emission from the excited singlet state. A 1:1 blend of **D2:A1** shows almost no PL prior to annealing. After annealing at 110 °C, some PL from both materials is observed. These observations, along with AFM images, indicate that the materials are very well mixed in the as-cast films, with a large donor and acceptor interfacial area and small domains of individual materials which results in efficient charge separation and almost complete PL quenching. Upon annealing, perhaps, the materials phase separate into domains significantly larger than the exciton diffusion length, precluding the quenching of a fraction of the excitons at the **D2: A1** interface. Absorbance and PL of blends using the n-hexyl derivative, **A2** were also investigated, as shown in Figure 2c,d, respectively. The behavior of these blends closely resembles the films prepared with **A1**, where the PL from the acceptor is quenched upon mixing with **D2**, and partially recovered upon annealing.

The morphology of films comprising 1:1 mixtures of **D2:A1** and **D2:A2** were examined by AFM and are reported in Figure 3. As-cast films of **D2:A1** (Figure 3a) are fairly smooth (rms roughness of 0.7 nm) and show small, raised, oblong features which are approximately 172 nm long, 80 nm wide and protrude 2.2 nm from the surface. These features are not apparent in films of **D2** or mixtures of **D2** with other materials, thus we speculate that the oblong domains are comprised largely of **A1**. As-cast films of **D2:A2** (Figure 3b) are somewhat rougher (rms roughness of 2.3 nm) and do not shown distinct features. After annealing at 110 °C, the films become considerably rougher. The roughness of the **D2:A1** (Figure 3c) film increases to 19 nm, while the roughness of the **D2:A2** (Figure 3d) film increases to 4.2 nm.

BHJ solar cells were prepared using the architecture ITO/PEDOT:PSS/**D2:A1**/Al. The current density−voltage (J−V) characteristics of devices using different blend ratios and different annealing temperatures are reported in Figure 4, while their device parameters are quantified in Table 1. With the

dx.doi.org/10.1021/am201304e | *ACS Appl. Mater. Interfaces* 2012, 4, 244−250

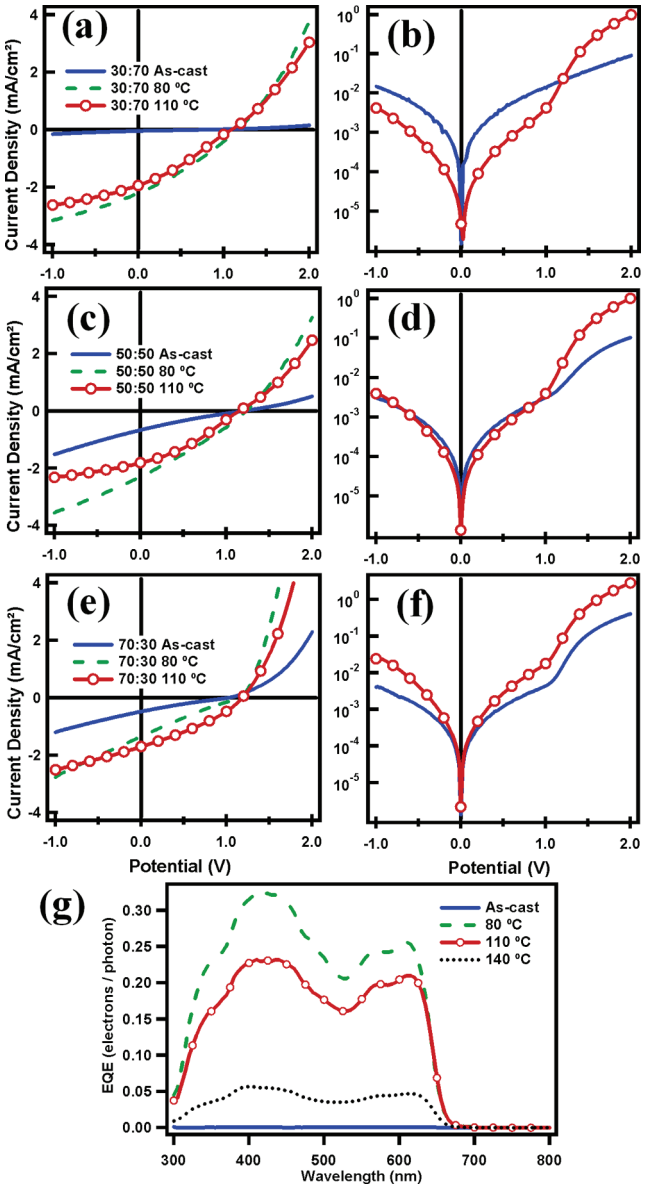

Figure 4. *J*–*V* characteristics of BHJ devices incorporating **D2**:**A1**. *J*–*V* curves were collected (a, c, e) under 100 mW/cm^2 simulated solar illumination and (b, d, f) in the dark for (a, b) 30:70, (c, d) 50:50, and (e, f) 70:30 donor:acceptor ratios. (g) EQE spectra of the 50:50 ratio annealed at various temperatures.

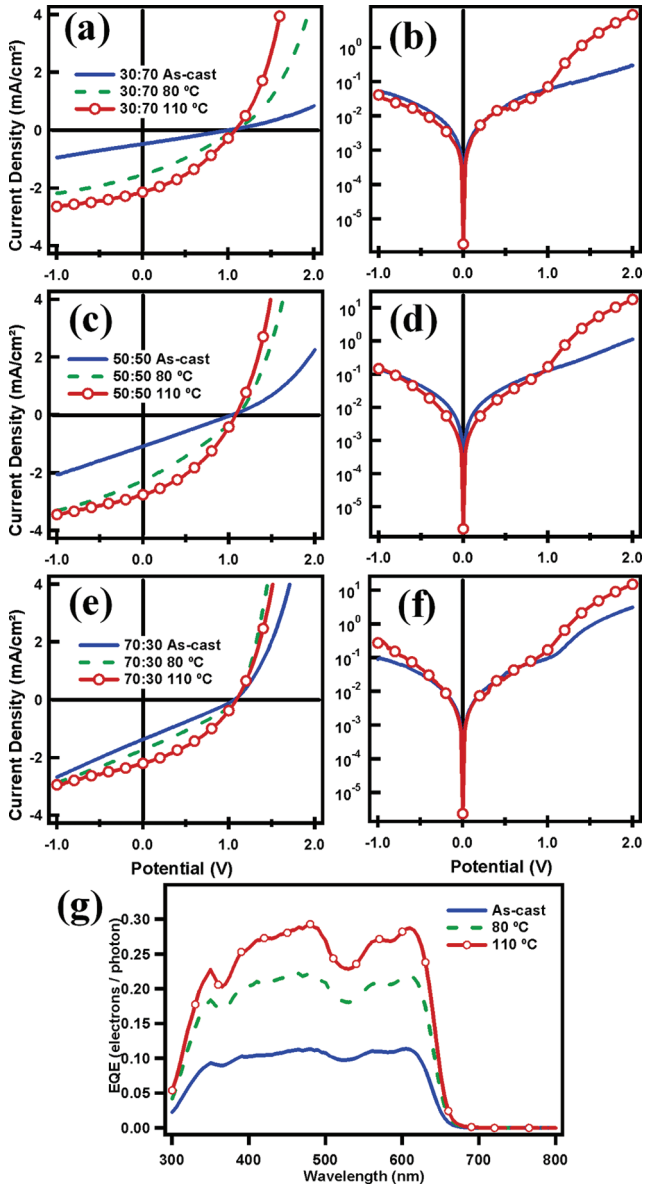

Figure 5. *J*–*V* characteristics of BHJ devices incorporating **D2**:**A2**. *J*–*V* curves were collected (a, c, e) under 100 mW/cm^2 simulated solar illumination and (b, d, f) in the dark for (a, b) 30:70, (c, d) 50:50 and (e, f) 70:30 donor:acceptor ratios. (g) EQE spectra of the 50:50 ratio annealed at various temperatures.

exception of the as-cast device using a 30:70 ratio, which showed little photovoltaic effect, the V_{OC} values are in the range of 1.02 to 1.23 V; relatively high values compared to those obtained using PCBM as an acceptor (~0.9 V), although somewhat smaller than the expected 1.4 V based on the LUMO of the acceptor. Because the work function (φ) of the Al (4.2 eV) is significantly lower than the LUMO of the acceptor (3.5 eV), it might seem that the cathode φ might limit the electrical potential developed in these devices, however, attempting to use Ba or LiF cathodes did not result in a V_{OC} or short circuit current density (J_{SC}) higher than the values observed when using Al.

Before thermal annealing, the devices exhibit rather poor performance. The 30:70 ratio produces almost no photocurrent (J_{SC} = 0.04 mA/cm^2), whereas the 50:50 and 70:30 ratios produce relatively small photocurrents (0.67 and 0.48 mA/cm^2, respectively) compared to a control device using PCBM as an acceptor at a 50:50 ratio (J_{SC} = 1.65 mA/cm^2). The currents and fill factors (FFs) produced by the devices are likely hindered by the high series resistance of 7844, 6126, and 1470 Ω cm^2, for the 30:70, 50:50, and 70:30 ratios, respectively.

Annealing causes considerable improvement in several aspects of the devices. After annealing at 80 °C for 10 min, the series resistance of all the devices drops by approximately an order of magnitude to 329, 555, and 207 Ω cm^2, while the J_{SC}'s increase to 2.2, 2.3, and 1.4 mA/cm^2 for the 30:70, 50:50, and 70:30 ratios, respectively. These changes are likely caused by an increase in phase separation and ordering of active materials, which provides interfaces for charge separation and pathways for carrier transport, similar to what has been previously observed in related BHJ devices.[27] Annealing at higher temperatures (110 °C) causes a decrease in the

dx.doi.org/10.1021/am201304e | ACS Appl. Mater. Interfaces 2012, 4, 244–250

Table 1. Device Characteristics of BHJ Solar Cells Using D2:A1 and D2:A2 Blends

acceptor	ratio (D:A)	annealing Temp (°C)	J_{SC} (mA/cm^2)	V_{OC} (V)	FF	PCE (%)	R_{series} (Ω cm^2)	R_{shunt} (Ω cm^2)
A1	30:70	as-cast	0.04	0.71	0.24	0.01	7844	2.0×10^5
A1	50:50	as-cast	0.67	1.19	0.21	0.17	6126	1.1×10^6
A1	70:30	as-cast	0.48	1.02	0.22	0.11	1470	7.2×10^5
PCBM	50:50	as-cast	1.65	0.87	0.27	0.39	4	5.9×10^4
A1	30:70	80	2.21	1.16	0.30	0.76	329	1.3×10^6
A1	50:50	80	2.30	1.23	0.28	0.80	555	2.0×10^6
A1	70:30	80	1.35	1.14	0.23	0.35	207	2.0×10^6
PCBM	50:50	80	8.70	0.92	0.44	3.48	2	2.6×10^5
A1	30:70	110	1.94	1.09	0.30	0.63	502	2.7×10^6
A1	50:50	110	1.81	1.15	0.33	0.69	497	2.2×10^6
A1	70:30	110	1.70	1.18	0.33	0.66	184	5.4×10^5
PCBM	50:50	110	9.26	0.84	0.48	3.72	2	4.0×10^5
A2	30:70	as-cast	0.47	0.99	0.26	0.12	2197	3.9×10^4
A2	50:50	as-cast	1.08	1.03	0.25	0.28	469	1.8×10^4
A2	70:30	as-cast	1.37	1.06	0.26	0.38	177	2.6×10^4
A2	30:70	80	1.54	1.08	0.29	0.49		
A2	50:50	80	2.27	1.10	0.29	0.73		
A2	70:30	80	1.73	1.09	0.30	0.55		
A2	30:70	110	2.14	1.08	0.35	0.81	52	5.4×10^4
A2	50:50	110	2.76	1.08	0.37	1.10	26	4.7×10^4
A2	70:30	110	2.20	1.09	0.36	0.87	33	3.0×10^4

photocurrent of the 30:70 and 50:50 blends to 1.94 and 1.81 mA/cm^2, respectively, whereas the 70:30 ratio increases to 1.7 mA/cm^2. The decrease in current of the 30:70 and 50:50 blends may stem from excessive phase separation, consistent with the large features and roughness apparent in the AFM image of the annealed film. The 70:30 ratio contains a larger amount of donor material that appears to have a higher thermal transition temperature. The as-cast devices exhibit meager *FF*'s of 0.24, 0.21, and 0.22 for the 30:70, 50:50, and 70:30 ratios, respectively, which show marginal improvement upon thermal annealing, increasing up to 0.30, 0.33, and 0.33, respectively after annealing at 110 °C. The optimum conditions are for a 50:50 ratio annealed at 80 °C, yielding J_{SC}, V_{OC}, FF, and PCE values of 2.3 mA/cm^2, 1.23 V, 0.28, and 0.80%, respectively. External quantum efficiencies (EQEs) of the devices show strong photocurrent response from 350 to 650 nm, which follows the absorption spectrum of the films.

On the basis of the high series resistance (R_{series}) of the **A1**-based devices, it appears that carrier transport may be hindered by the excessive bulk of the acceptor's insulating ethylhexyl chains, while at the same time, the drastic roughening of the films upon annealing indicates that a somewhat higher thermal transition temperature may be desirable to allow greater control over the morphology. For these reasons, the n-hexyl Vinazene analogue was explored, where the n-hexyl chain is smaller and less bulky, may allow greater ordering and result in higher thermal transition temperatures in the solid state.[35] Devices using the architecture ITO/PEDOT:PSS/**D2:A2**/Al were prepared; the *J*−*V* characteristics are reported in Figure 5 and the device characteristics are listed at the bottom of Table 1.

In general, changing from 2-ethylhexyl to n-hexyl substituted Vinazene has the expected effects, where the roughening upon thermal annealing is less drastic and the R_{series} of the devices is about an order of magnitude lower, indicative of more efficient carrier transport through the devices. This observation is consistent with changes in electron mobilities, which were calculated by fabricating electron-only diodes with films of **A1** and **A2** and fitting the *J*−*V* characteristics with a field-dependent variation of the Mott-Gurney relationship for space-charge limited current (SCLC).[36] SCLC data can be found in the Supporting Information (Figure S3). The zero-field electron mobility of **A1** is found to be 3.0×10^{-8} cm^2/(V s) with a field dependence coefficient (γ) of 5.9×10^{-4} (m/V)$^{1/2}$, which increases considerably to 8.6×10^{-6} cm^2/(V s) with a much smaller γ of 9×10^{-5} (m/V)$^{1/2}$ after annealing at 110 °C. The n-hexyl derivative is found to have a much larger electron mobility of 1.1×10^{-6} cm^2/(V s) or 6.3×10^{-5} cm^2/(V s) before or after annealing, respectively, with $\gamma = 4.8 \times 10^{-4}$ or 9×10^{-5} (m/V)$^{1/2}$, respectively. Additionally, the J_{SC} and FF values of the **D2:A2** devices were generally higher, whereas the V_{OC} values were slightly lower (in the range of 0.99 to 1.10 V). It appears that the improved packing and morphology of the n-hexyl derivative allow for larger J_{SC} and FF, however, these changes in packing also seem to have the unwanted effect of an upward shift in the HOMO energy level, as evidenced by the decrease in V_{OC}.

The specific relationships between blend ratio and annealing were similar to those observed in the **A1** devices. In the as-cast films, the blend with lowest donor concentration showed the smallest photocurrent (0.47 mA/cm^2 for the 30:70 blend compared to 1.08 and 1.37 for the 50:50 and 70:30 ratios, respectively). Compared to the 2-ethylhexyl derivative, annealing had similar effects on the J_{SC}, R_{series} and FF, though the optimum annealing temperature was found to be higher. The J_{SC}'s increased with annealing temperature to 1.54, 2.27, and 1.73 mA/cm^2 at 80 °C and 2.14, 2.76, and 2.20 mA/cm^2 at 110 °C, the series resistances decreased from 2197, 469, 177 Ω cm^2 in the as-cast films to 52, 26, 33 Ω cm^2 after annealing at 110 °C, whereas the FF values increased from 0.26, 0.25, and 0.26 in the as-cast films to 0.35, 0.37, and 0.36 after annealing at 110 °C for the 30:70, 50:50, and 70:30 ratios, respectively. The optimum devices using **D2:A2** system were prepared using a 50:50 ratio annealed at 110 °C and showed J_{SC}, V_{OC}, FF, and PCE values of 2.8 mA/cm^2, 1.08 V, 0.33, and 1.1%, respectively.

Table 2. Device Characteristics of Solution-Processed Bilayer Solar Cells Using D2 and A1 Layers

donor Spin rate (rpm)	donor thickness (nm)	acceptor spin rate (rpm)	acceptor thickness (nm)	J_{SC} (mA/cm^2)	V_{OC} (V)	*FF*	PCE (%)	R_{series} (Ω cm^2)	R_{shunt} (Ω cm^2)
1000	54	2000	30	0.57	1.19	0.39	0.26	30	2.8×10^5
2000	42	2000	30	1.13	1.23	0.49	0.69	23	1.3×10^5
4000	33	2000	30	1.11	1.23	0.47	0.65	34	6.6×10^4
2000	42	1000	39	1.43	1.25	0.43	0.77	105	1.0×10^5
2000	42	4000	23	0.77	1.18	0.44	0.40	26	9.1×10^4

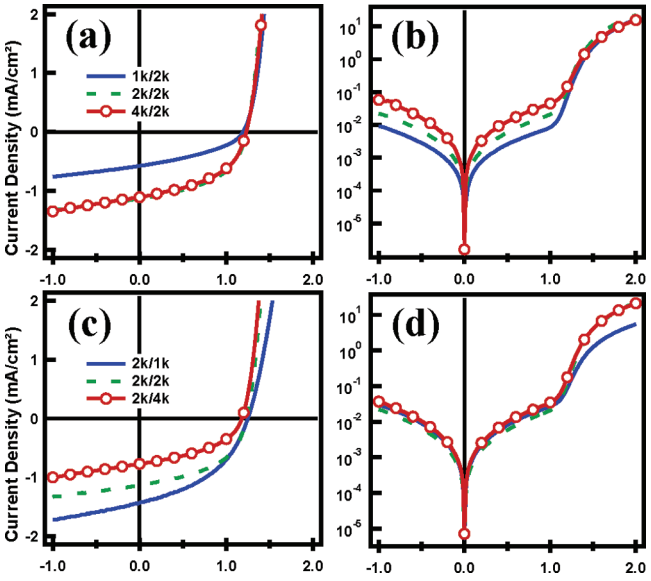

Figure 6. *J*–*V* characteristics of bilayer devices **D2**:**A1**. *J*–*V* curves were collected (a, c) under 100 mW/cm^2 simulated solar illumination and (b, d) in the dark for cells with (a, b) variable donor thickness and (c, d) variable acceptor thickness.

Solution-processed bilayer devices were also explored by depositing a layer of pure **D2** from a 5 mg/mL solution in chloroform, followed by a layer of **A1** from a 5 mg/mL solution in methyl ethyl ketone (MEK), similar to a previously reported procedure.[37,38] The spin rates were adjusted to control the thickness of each layer. The current voltage characteristics are reported in Figure 6 while the device characteristics are listed in Table 2. In general, the bilayer devices produce smaller J_{SC} values and larger FF values than their BHJ counterparts, which is consistent with limited interfacial area provided by the more planar donor:acceptor interface and direct route for carrier extraction. The optimum device was found to have a donor thickness of ∼42 nm and an acceptor thickness of ∼39 nm, yielding a J_{SC}, V_{OC}, FF, and PCE of 1.25 mA/cm^2, 1.25 V, 0.43, and 0.77%, respectively. Thermal or solvent annealing of the partially fabricated or complete devices was not found to provide significant benefit, nor was modifying the donor layer using solvent additives.

CONCLUSIONS

A DPP donor material with an appropriately chosen LUMO (**D2**) is found to work well with Vinazene-based acceptors in BHJ and bilayer type solar cells, yielding a V_{OC} of up to 1.25 V and PCE of up to 1.1%. Both materials are easily synthesized from relatively inexpensive starting materials. BHJ devices incorporating the n-hexyl Vinazene are found to have more favorable morphology than the 2-ethylhexyl derivative, while such devices exhibit improved series resistance, J_{SC}, and FF, though the 2-ethylhexyl derivative produces a slightly higher V_{OC}. The photocurrent generation in these solar cells is small and may be limited by the development of percolation pathways or by large domain sizes and small interfacial areas between donor and acceptor phases. Solution processed bilayer devices were realized by depositing a **D2** layer from chloroform followed by an **A1** layer deposited from MEK. These devices showed improved FF values compared to the BHJ devices, though with reduced photocurrents and lower PCEs.

EXPERIMENTAL METHODS

D1 and **D2** were synthesized according to refs 27 and 28, respectively. Vinazene derivatives **A1** and **A2** were synthesized according to ref 22. Solar cells were fabricated by spin-casting the BHJ active layer onto a 55 nm layer of PEDOT:PSS (H.C. Stark Baytron P 4083) atop Corning 1737 glass patterned with 140 nm of ITO (Thin Film Devices). PEDOT:PSS is poly(3,4-ethylenedioxythiophene) poly(styrenesulfonate). Unless otherwise stated, the BHJ layer was spin-cast from chloroform at a total solids concentration of 16.7 mg mL^{-1}. The active layer thicknesses were determined using an Ambios XP-100 Stylus profilometer. Solar cells were characterized under simulated 100 mW/cm^2 AM1.5G irradiation from a 300W Xe arc lamp with an AM1.5 global filter. Simulator irradiance was characterized using a calibrated spectrometer, and illumination intensity was set using an NREL certified silicon diode with an integrated KG1 optical filter; spectral mismatch factors were calculated to be less than 10%. Quantum efficiencies were measured with a Xe lamp, monochromator, optical chopper, and lock-in amplifier; photon flux was determined by a calibrated silicon photodiode. Device fabrication and testing were done under inert atmosphere in a nitrogen filled glovebox. UV/vis absorption spectra were measured on a Shimadzu 2401 diode array spectrometer. PL spectra were collected using a Photon Technology International 1860 Fluorimeter. AFM images were collected in air under ambient conditions using the Innova scanning probe microscope (Bruker Nano). Silicon probes with resonant frequencies of 75 kHz (Budget Sensors) were used for tapping mode AFM measurements.

ASSOCIATED CONTENT

Supporting Information

Cyclic voltammograms of **D1** and **D2**, device characteristics of **D1**, and *J*–*V* characteristics of single-carrier diodes used to extract charge carrier mobilities. This material is available free of charge via the Internet at http://pubs.acs.org/.

AUTHOR INFORMATION

Corresponding Author

*E-mail: quyen@chem.ucsb.edu.

ACKNOWLEDGMENTS

B.W. thanks the NSF ConvEne IGERT program for financial support. C.K. is supported by the Office of Naval Research. T.Q.N. thanks the Camille Dreyfus Teacher-Scholar Awards and the Alfred P. Sloan Foundation program for the financial support. X.H. and A.S. acknowledge that this publication was partially based on work supported by the Center for Advanced

Molecular Photovoltaics (CAMP) (Award KUS-C1-015-21), made by King Abdullah University of Science and Technology (KAUST).

REFERENCES

(1) Chen, H.-Y.; Hou, J.; Zhang, S.; Liang, Y.; Yang, G.; Yang, Y.; Yu, L.; Wu, Y.; Li, G. *Nat. Photonics* **2009**, *3*, 649−653.
(2) Riede, M.; Uhrich, C.; Timmreck, R.; Widmer, J.; Wynands, D.; Levichkova, M.; Furno, M. ; Schwartz, G. ; Gnehr, W. ; Pfeiffer, M.; Leo, K. In *2010 35th IEEE Photovoltaic Specialists Conference (PVSC)*; IEEE: Piscataway, NJ, 2010; p 513−517.
(3) Heliatek GmbH press release. http://www.heliatek.com/news-19 (accessed Aug 21, 2011).
(4) Konarka Technologies Inc. press release. http://www.konarka.com/index.php/site/pressreleasedetail/konarkas_power_plastic_achieves_world_record_83_efficiency_certification_fr (accessed Aug 21, 2011).
(5) http://en.wikipedia.org/wiki/File:PVeff%28rev110408U%29.jpg (accessed Aug 21, 2011)
(6) Dennler, G; Scharber, M. C.; Brabec, C. J. *Adv. Mater.* **2009**, *21*, 1323−1338.
(7) Li, C; Liu, M.; Pschirer, N. G.; Baumgarten, M.; Müllen, K. *Chem. Rev.* **2010**, *110*, 6817−6855.
(8) Helgesen, M.; Søndergaard, R.; Krebs, F. C. *J. Mater. Chem.* **2010**, *20*, 36−60.
(9) Walker, B.; Kim, C.; Nguyen, T.-Q. *Chem. Mater.* **2011**, *23*, 470−482.
(10) Rousseau, T.; Cravino, A.; Ripaud, E.; Leriche, P.; Rihn, S.; De Nicola, A.; Ziessel, R.; Roncali, J. *Chem. Commun.* **2010**, *46*, 5082−5084.
(11) Bagnis, D.; Beverina, L.; Huang, H.; Silvestri, F.; Yao, Y.; Yan, H.; Pagani, G. A.; Marks, T. J.; Facchetti, A. *J. Am. Chem. Soc.* **2010**, *132*, 4074−4075.
(12) Burckstummer, H.; Kronenberg, N. M.; Gsanger, M.; Stolte, M.; Meerholz, K.; Wurthner, F. *J. Mater. Chem.* **2010**, *20*, 240−243.
(13) Yin, B.; Yang, L.; Liu, Y.; Chen, Y.; Qi, Q.; Zhang, F.; Yin, S. *Appl. Phys. Lett.* **2010**, *97*, 023303.
(14) Wei, G.; Wang, S.; Sun, K.; Thompson, M. E.; Forrest, S. R. *Adv. Energy Mater.* **2011**, *1*, 184−187.
(15) Liu, Y.; Wan, X.; Wang, F.; Zhou, J.; Long, G.; Tian, J.; You, J.; Yang, Y.; Chen, Y. *Adv. Energy Mater.* **2011**, *1*, 771−775.
(16) Shang, H.; Fan, H.; Liu, Y.; Hu, W.; Li, Y.; Zhan, X. *Adv. Mater.* **2011**, *23*, 1554−1557.
(17) Welch, G. C.; Perez, L. A.; Hoven, C. V.; Zhang, Y.; Dang, X.-D.; Sharenko, A.; Toney, M. F.; Kramer, E. J.; Nguyen, T.-Q.; Bazan, G. C. *J. Mater. Chem.* **2011**, *21*, 12700−12709.
(18) Zhou, J.; Wan, X.; Liu, Y.; Long, G.; Wang, F.; Li, Z.; Zuo, Y.; Li, C.; Chen, Y. *Chem. Mater.* **2011**, *23*, 4666−4668.
(19) Scott, L. T. *Angew. Chem., Int. Ed.* **2004**, *43*, 4994.
(20) Anthony, J. E. *Chem. Mater.* **2011**, *23*, 583−590.
(21) Ooi, Z. E.; Tam, T. L.; Shin, R. Y. C.; Chen, Z. K.; Kietzke, T.; Sellinger, A.; Baumgarten, M.; Müllen, K.; deMello, J. C. *J. Mater. Chem.* **2008**, *18*, 4619−4622.
(22) Shin, R. Y. C.; Sonar, P.; Siew, P. S.; Chen, Z.-K.; Sellinger, A. *J. Org. Chem.* **2009**, *74*, 3293−3298.
(23) Schubert, M.; Yin, C.; Castellani, M.; Bange, S.; Tam, T. L.; Sellinger, A.; Horhold, H.-H.; Kietzke, T.; Neher, D. *J. Chem. Phys.* **2009**, *130*, 094703.
(24) Inal, S.; Schubert, M.; Sellinger, A.; Neher, D. J. *Phys. Chem. Lett.* **2010**, *1*, 982−986.
(25) Sonar, P.; Ng, G.-M.; Lin, T. T.; Dodabalapur, A.; Chen, Z.-K. *J. Mater. Chem.* **2010**, *20*, 3626−3636.
(26) Brunetti, F. G.; Gong, X.; Tong, M.; Heeger, A. J.; Wudl, F. *Angew. Chem., Int. Ed.* **2010**, *49*, 532−536.
(27) Walker, B.; Tamayo, A. B.; Dang, X. D.; Zalar, P.; Seo, J. H.; Garcia, A.; Tantiwiwat, M.; Nguyen, T.- Q. *Adv. Funct. Mater.* **2009**, *19*, 3063−3069.
(28) Kim, C.; Tantiwiwat, M.; Sherman, J. B.; Tamayo, A. B.; Parkin, S. R.; Wu, G.; Nguyen, T.-Q. Submitted to *Chem. Mater.*
(29) Lee, C; Yang, W.; Parr, R. G. *Phys. Rev. B* **1988**, *37*, 785−789.
(30) Erb, T.; Zhokhavets, U.; Gobsch, G.; Raleva, S.; Stuhn, B.; Schilinsky, P.; Waldauf, C.; Brabec, C. J. *Adv. Funct. Mater.* **2005**, *15*, 1193−1196.
(31) Erb, T.; Zhokhavets, U.; Hoppe, H.; Gobsch, G.; Al-Ibrahim, M.; Ambacher, O. *Thin Solid Films* **2006**, *511−512*, 483−485.
(32) Chirvase, D.; Parisi, J.; Hummelen, J. C.; Dyakonov, V. *Nanotechnology* **2004**, *15*, 1317−1323.
(33) Scharber, M. C.; Muhlbacher, D.; Koppe, M.; Denk, P.; Waldauf, C.; Heeger, A. J.; Brabec, C. J. *Adv. Mater.* **2006**, *18*, 789−794.
(34) Jakubiak, R.; Collison, C. J.; Wan, W. C.; Rothberg, L. J. *J. Phys. Chem. A.* **1999**, *103*, 2394−2398.
(35) Tashiro, K.; Ono, K.; Minagawa, Y.; Kobayashi, M.; Kawai, T.; Yoshino, K. *J. Polym. Sci., Part B: Polym. Phys.* **1991**, *29*, 1223−1233.
(36) Blom, P. W. M.; de Jong, M. J. M.; van Munster, M. G. *Phys. Rev. B* **1997**, *55*, R656−R659.
(37) Schubert, M.; Yin, C.; Castellani, M.; Bange, S.; Tam, T. L.; Sellinger, A.; Hörhold, H.-H.; Kietzke, T.; Neher, D. *J. Chem. Phys.* **2009**, *130*, 094703.
(38) Inal, S.; Castellani, M.; Sellinger, A.; Neher, D. *Macromol. Rapid Commun.* **2009**, *30*, 1263−1268.